Appl Phys B (2009) 95: 273–280
DOI 10.1007/s00340-009-3424-0

Applied Physics B
Lasers and Optics

A linear optical method for measuring the carrier-envelope phase drift

M. Görbe · C. Grebing · G. Steinmeyer · K. Osvay

Received: 30 September 2008 / Published online: 5 March 2009

Abstract The carrier-envelope offset frequency of a laser oscillator is determined from the visibility of spectrally resolved fringes in a combined two-path multiple-path interferometer. At maximum visibility the pulses have zero carrier-envelope phase drift, while the visibility becomes zero for uncorrelated pulses. The method is widely independent of bandwidth and pulse energy. The effects of carrier-envelope offset phase noise, finite detection time, and dispersion are also discussed.

PACS 42.60.Da · 42.65.Re

1 Introduction

Measurement and stabilization of the carrier-envelope offset (CEO) frequency [1–3] have opened a new avenue towards attosecond physics [4, 5], phase-sensitive nonlinear optics [6], and frequency metrology at unprecedented levels of precision [7–9]. The key invention enabling all these applications is the f-to-$2f$ interferometer [1–3], an interferometer in which frequency-doubled modes from the long-wavelength edge of a frequency comb are brought into interference with high-frequency components of the same comb, yielding the CEO frequency as their respective beat frequency. Originally, this method was proposed and demonstrated for few-cycle oscillators [2] and later adapted to amplifier systems with repetition rates that render radio-frequency heterodyne schemes impossible [10, 11]. However, all of these approaches toward CEO measurement, including sum and difference frequency generation schemes [5, 6], work only if the bandwidth of the mode-locked fundamental pulse is about one octave wide. Sub-division schemes have been suggested as a resort, but any factor two in bandwidth reduction requires an additional sub-division stage, which strongly discourages their use in most applications. Alternatively, the output spectrum of the laser may be broadened by nonlinear optical processes prior to the f-to-$2f$ interferometer, e.g., by supercontinuum (SC) generation in microstructure fibers [2]. While this works fairly well for pulses of 10–20 fs pulse duration, there are no reports of successful application of SC broadening of 100 fs pulses for CEO sensitive applications. Even though this has never been fully clarified, this problem may be related to a loss of spectral coherence in the extreme broadening required to generate an octave-spanning spectrum from a 100 fs pulse [12]. Additionally, even for 10 fs pulses, SC generation may introduce noise and drift [13, 14] and is therefore often regarded as an inferior solution as compared to direct stabilization schemes [15, 16]. Despite its proven success, f-to-$2f$ interferometry has to be considered to be quite demanding, both in terms of bandwidth and power levels compatible with the nonlinear processing steps required for generating the f and the $2f$ components. Therefore, f-to-$2f$ interferometry has found widespread use for Ti:sapphire lasers and fiber lasers only [17], effectively excluding the CEO frequency of many other femtosecond oscillators from measurement.

In the following we introduce a novel linear optical procedure for measurement of the CEO frequency of femtosec-

M. Görbe and C. Grebing have equally contributed to this paper.

M. Görbe · K. Osvay (✉)
Department of Optics and Quantum Electronics, University of Szeged, P.O. Box 406, Szeged 6701, Hungary
e-mail: osvay@mbi-berlin.de

C. Grebing · G. Steinmeyer · K. Osvay
Max Born Institute, Max-Born-Str. 2a, 12489 Berlin, Germany

ond oscillators. Our method is interferometric and related to the first published method for demonstrating the carrier-envelope phase (CEP) drift [18]. Other than the latter, however, no nonlinear conversion step is required [19]. Specifically, we employ spectrally and spatially resolved interferometry (SSRI), which has been proven a powerful technique for dispersion measurements [20–24]. The major advantage of SSRI consists of the simultaneous detection of many interferograms, allowing for efficient noise suppression and averaging in a single acquisition process. The SSRI setup consists of a two-beam interferometer equipped with an imaging spectrograph. The interference pattern is imaged onto the input slit of the spectrograph, such that spatially (along the slit) and spectrally resolved interference fringes are formed on a 2D detector (CCD camera) placed in the image plane of the spectrograph. For dispersion measurements, only slope and curvature of the interference fringes are relevant for calculating the group delay and its dispersion. The absolute fringe phase, in contrast, may experience drift and is typically discarded, which makes it difficult to directly extract phase information from such a setup. In the following, we will deduce a method to decode carrier-envelope phase information from the visibility of an SSRI interferogram. The technique relies on linear interference only; it is therefore applicable to laser pulses from the UV to the far IR, as well as for picosecond pulse duration.

2 Theoretical description

Let us first consider a standard SSRI based on a Mach–Zehnder interferometer illuminated by a femtosecond pulse (Fig. 1a). After beamsplitter BS1, the reference pulse with spectral power density $I_R(\omega)$ propagates undisturbed in one arm of the interferometer while the sample pulse [$I_S(\omega)$] experiences a phase shift from the sample in the other interferometer arm. The spectral phase difference between the two pulses is best described as a Taylor series around a center frequency of ω_0:

$$\begin{aligned}\Delta\varphi(\omega) &= \varphi_R(\omega) - \varphi_S(\omega)\\ &= \Delta\varphi(\omega_0) + \frac{d\Delta\varphi}{d\omega}(\omega-\omega_0)\\ &\quad + \frac{1}{2}\frac{d^2\Delta\varphi}{d\omega^2}(\omega-\omega_0)^2 + \cdots. \end{aligned} \tag{1}$$

Here $\Delta\varphi(\omega_0)$ denotes a constant phase offset between the two arms; the first-order derivative describes a timing difference; higher-order derivatives denote the dispersion. Note that under idealized conditions (vacuum, no mirror dispersion) the latter exclusively stems from the material in one arm, whereas the two leading terms can also occur in an empty interferometer.

Temporally overlapping the pulses at the second beamsplitter ($d\Delta\varphi/d\omega = 0$) and tilting their phase fronts at an angle of ε (Fig. 1b), interference fringes are formed along the y axis parallel to the input slit of the spectrograph. These spectral and spatial interference fringes are described by the intensity distribution

$$\begin{aligned}I(y,\omega) &= \left|E_S(\omega) + E_R(\omega)\right|^2\\ &= I_S(\omega) + I_R(\omega) + 2\sqrt{I_S(\omega)\cdot I_R(\omega)}\\ &\quad \times \cos\left(\Delta\varphi(\omega) + \varepsilon\frac{\omega}{c}(y-y_0)\right), \end{aligned} \tag{2}$$

where y_0 is the height at which the temporal difference is zero between the ω_0 frequency components of the pulses from the two arms [25]. For this configuration, the differential phase is composed of an offset and dispersion contributions of second order and higher

$$\Delta\varphi(\omega) = \Delta\varphi_{\mathrm{CE}}^{R-S} + D(\omega), \tag{3}$$

where the dispersive part $D(\omega)$ describes the shape of the fringes [21, 23] and $\Delta\varphi_{\mathrm{CE}}^{R-S}$ is the carrier-envelope phase

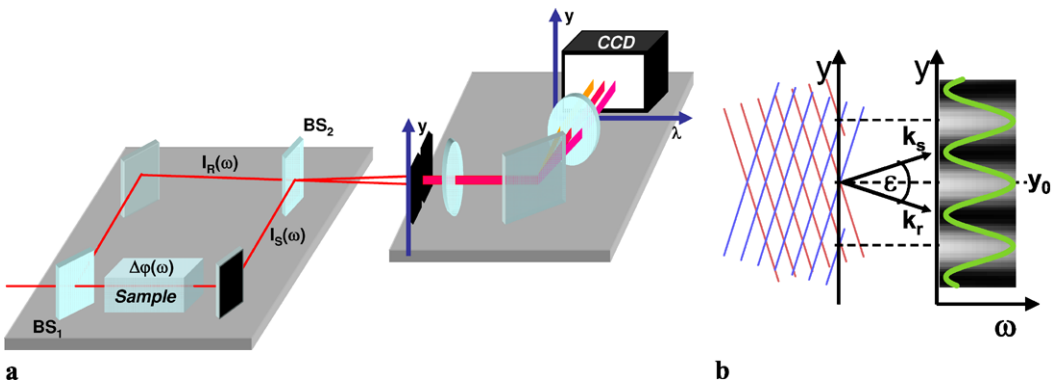

Fig. 1 A spectrally and spatially resolved interferometer (**a**) and the formation of spectrally and spatially resolved interference fringes (**b**). The phase-shifting element in the sample arm represents the relative phase difference between the sample and reference pulses

difference between the reference and sample pulse induced by single transmission through the sample. The carrier-envelope phase (CEP) therefore determines the offset of the entire fringe pattern. In other words, once the interferometer has been aligned, a change in the initial phase difference between the reference and sample pulses results in a vertical shift of the entire fringe pattern.

While in two-path interferometry the initial phase change and therefore $\Delta\varphi_{\mathrm{CE}}^{R-S}$ arises only once upon transmission through the sample, pulses traveling through a multi-path interferometer, e.g., inside a Fabry–Pérot type laser cavity, will experience a material induced phase change twice upon every round trip, causing a continuous phase slippage of the carrier below the envelope structure of the pulses in the train. This pulse to pulse CEP drift, which is sometimes also called the *carrier-envelope offset* (*CEO*) *phase*, is

$$\Delta\varphi_{\mathrm{CE}} = \varphi'_{\mathrm{CE}} - \varphi_{\mathrm{CE}} = \varphi''_{\mathrm{CE}} - \varphi'_{\mathrm{CE}} = \cdots, \tag{4}$$

where the φ_{CE}, φ'_{CE}, φ''_{CE} etc. denote the carrier-envelope phase of the first, the second, the third etc. pulse.

Formally, the CEP slippage rate can be written as a fraction of the repetition rate f_{rep},

$$f_{\mathrm{CEO}} = \frac{\Delta\varphi_{\mathrm{CE}}}{2\pi} \cdot f_{\mathrm{rep}}. \tag{5}$$

In the frequency domain, f_{CEO} is readily identified as the zero offset of the longitudinal laser mode comb [1]. In the following, we will therefore refer to this frequency as the carrier-envelope offset (CEO) frequency f_{CEO}. Note that for constant repetition rate, the CEO frequency is strictly proportional to the pulse-to-pulse CEP difference $\Delta\varphi_{\mathrm{CE}}$.

Let us now consider a situation, where we have several replicas at identical timing but at a constant phase difference in one arm of a Mach–Zehnder interferometer while the other arm hosts only one single reference pulse. If interference between the replicas is constructive, they all interfere in the same way with the reference pulse from the other arm. This maximum constructive superposition of the replicas then yields the strongest possible visibility of the SSRI interference pattern. This situation is changed when the replicas have different phases, i.e., each of them interferes with the reference in a different way, which reduces the visibility of the fringe pattern. This is the key observation to understanding our interferometric scheme. Any deviation from an identical relative phase of the replicas in one arm will reduce the obtainable visibility of the resulting SSRI fringe pattern.

It is important to understand that the relative phase between the two arms of the Mach–Zehnder interferometer does not affect the visibility of the resulting fringe pattern. As was shown above, a phase shift will only translate into an equal vertical shift of all fringe patterns involved, leaving the maximum and minimum intensities unchanged. Therefore, SSRI here serves a purpose different from dispersion measurements, effectively encoding relative phase differences between the replicas in the visibility and effectively removing drift of the Mach–Zehnder interferometer as an error source.

To this end, the basic function of our concept and the role of SSRI should be clear. However, it is still unclear how oscillator laser pulses that are typically separated by some 10 nanosecond timing difference are brought on top of each other in the sample arm of the interferometer. In the following it will be described how a resonant ring resonator in the sample arm may serve this purpose and the resulting combination of a two-path and a multi-path interferometer can be used to measure the relative CEP between subsequent pulses of a laser cavity.

3 SSRI with a resonant ring

Figure 2 shows the complete architecture of our interferometric CEP drift measurement set-up, with a ring resonator inside the sample arm of the Mach–Zehnder interferometer. The total length of the resonator should match the repetition rate of the pulse train (or one of its integer multiples). Let first the Mach–Zehnder interferometer be symmetrical; that

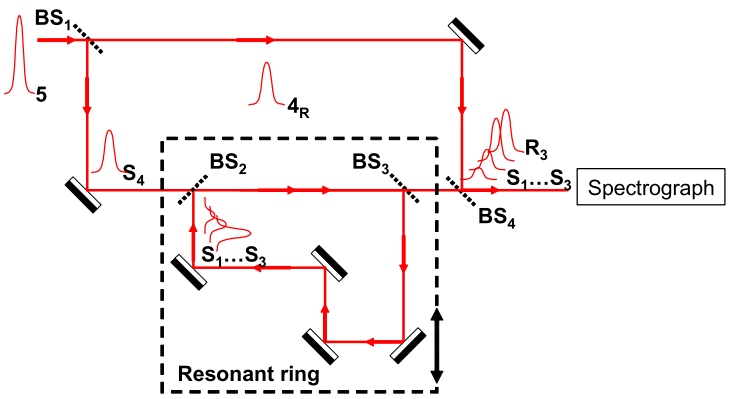

Fig. 2 A setup for linear detection of CEO phase with a Mach–Zehnder interferometer

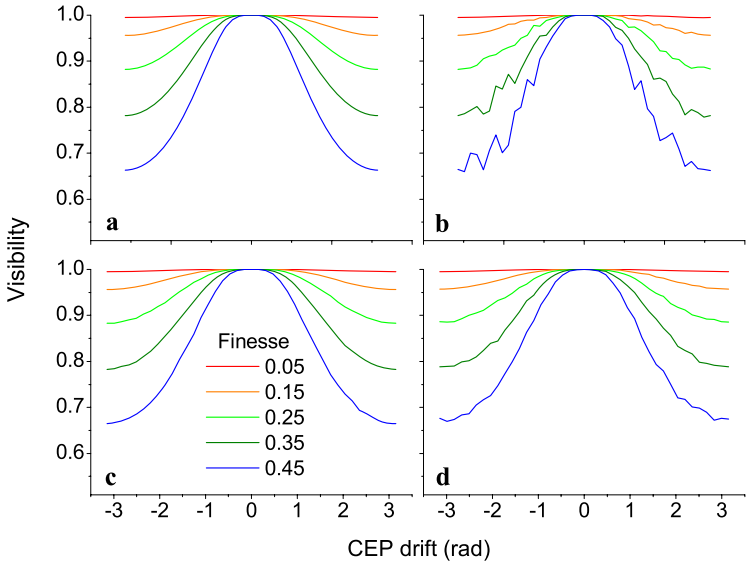

Fig. 3 Visibility of the SSRI fringes from a resonant ring as a function of CEP drift, at different resonator finesses, integration time and CEP noises. Colors show variation of finesse parameter. The noise range around the value of CE phase is 0 rad (**a**), 200 mrad (**b**, **c**), and 600 mrad (**d**). The integration time corresponds to $n = 1$ pulse (**a**, **b**) and $n = 100$ pulses (**c**, **d**)

is, the optical path length in the reference arm equals to the optical path length of the sample arm excluding the ring. Since the remnants of all the subsequent (sample) pulses from the pulse train are circulating in the ring resonator, they appear at the same time at the output of the ring and interfere with the same pulse from the reference arm of the interferometer. Hence, the resulting interference pattern is constructed by the reference pulse R_3 and sample pulse S_3, R_3 and S_2, R_3 and S_1, etc. Generally speaking, if there are k detectable pulses at the output of the ring resonator, the interference pattern is described by:

$$I_{\mathrm{MZ+Ring}}(y,\omega) = \big|E_{S1}(\omega) + E_{S2}(\omega) + E_{S3}(\omega) + \cdots + E_{Sk}(\omega) + E_{Rk}(\omega)\big|^2, \tag{6}$$

where the phase difference between the reference and the sample pulses are characteristic to the CE phase difference of $\Delta\varphi_{\mathrm{CE}}^{R-S1}$, $\Delta\varphi_{\mathrm{CE}}^{R-S2}$, $\Delta\varphi_{\mathrm{CE}}^{R-S3}$, etc., respectively, again. Since the intensity of the pulses circulating in the ring decreases round by round, their contribution to the final pattern is also degraded. That is, the number of pulses forming detectable interference fringes can be controlled by the reflection of BS_2 and BS_3. In what follows, the product of the amplitude reflection of BS_2 and BS_3 will be called the finesse of the resonator ring.

4 Simulations

So far we have assumed a perfect interferometer with perfectly matched arm lengths, which appears virtually impossible to align and maintain within this state for any reasonable amount of time. For a better understanding of the characteristics of the combined interferometer and the influence of length variations, we have performed a series of numerical simulations. These simulations presume a mode-locked Ti:sapphire laser with central wavelength of 803 nm and a repetition rate of 87.4 MHz as the laser source to carefully match our experimental conditions (cf. Sect. 5).

In the simulations we either computed the visibility of the fringe pattern in dependence of CEP drift for a series of intracavity finesse parameters $F = (R_{\mathrm{BS2}} R_{\mathrm{BS3}})^{1/2}$ (Figs. 3, 5, and 6) or in dependence of wavelength for a series of CEP slippage rates (Figs. 4 and 6). All these simulations indicate a favorable influence of a large finesse, resulting in contrasted visibility values for varying CEP.

4.1 The effect of integration time and CEO phase noise

To bring the model as close to reality as possible, as a first step, the finite integration time of the detector of the imaging spectrograph and the noise of the CEO phase [13, 14, 26] are taken into account.

Figure 3a shows an ideal case when the dependence of visibility on the CEP drift is calculated from single interferograms (see (6)) without any disturbing effect. However, the CEO frequency of a phase stabilized oscillator is always strongly affected by environmental influences. To analyze the influence of CE phase jitter mechanism during the measurement interval, we computed the resulting phase dependence of the visibility pattern assuming a CEP jitter as randomly distributed values within a certain interval. At a jitter range of ± 100 mrad (Fig. 3b), one observes a dramatic raggedness of the visibility curve.

A commercial high resolution CCD camera is always relatively slow. This means that the captured image consists not only of the interferogram described by (6), but also of subsequent ones. To account for this effect, a total of $n = 100$ computations was averaged and is shown in

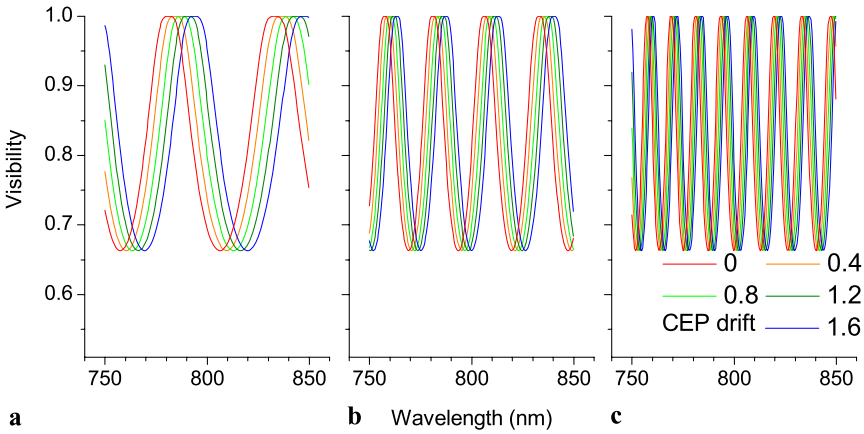

Fig. 4 Spectral dependence of the fringe visibility in the mismatched ring interferometer. (**a**) Mismatch between ring interferometer and laser master cavity $\Delta l = 12.5$ µm, (**b**) 25 µm, (**c**) 50 µm. Colors encode the CEP-drift in the master cavity

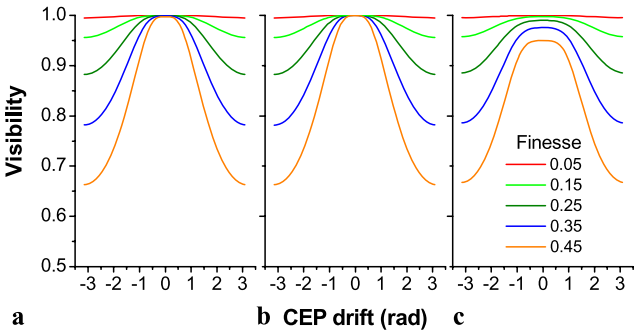

Fig. 5 Visibility of the SSRI fringes from a resonant ring as a function of CEO phase, at different resonator finesses. The resonator length fluctuation range is ±10 nm (**a**), ±20 nm (**b**), and ±100 nm (**d**). All other simulation parameters are unchanged

Fig. 3c under the same phase jitter conditions as for Fig. 3b. As one sees, the raggedness of the curves vanishes with an increased number of averages. The visibility curves are still relatively smooth for the rather large phase jitter interval of ±300 mrad (Fig. 3d).

As the situation analyzed here corresponds to an averaging time of only about 1 µs, whereas typical experimental situations correspond to about 1 million shots to be averaged, the long integration time of the camera should not affect our experiments. On the other hand, however, phase variations on the order of several 100 mrad have to be considered as rather large, such that one can conclude that phase jitter effects should not corrupt interpretation of the data as long as the acquisition times of the interferometer remain in the few millisecond range.

4.2 The effect of resonator length mismatch

Apart from jitter mechanisms, it also appears virtually impossible to align the length of two interferometers within a fraction of a wavelength and maintain this match without independent active stabilization. We therefore numerically investigated the characteristics of our interferometer set-up assuming a mismatch between the ring interferometer and the master laser cavity of several micrometers, which is shown in Fig. 4. Under a coarse ring length mismatch Δl of several wavelengths, fringe visibility becomes a function of wavelength, with approximately sinusoidal spectral dependence for the low-finesse cases considered here. These visibility curves clearly resemble the signals in spectral interferometry, with a period $\Delta\nu$ given by $c/\Delta l$. It is important to note that it is the fringe visibility but not the fringes themselves which encodes the phase information. In fact, the visibility is easy to retrieve as the amplitude of the fringe pattern but independent of the fringe positions. While the resonator mismatch dictates the period of the fringe pattern, the CE phase is encoded as the offset of this visibility comb. This very clearly resembles the frequency comb [1, 9] and its carrier-envelope offset frequency, yet this information is now encoded in the visibility of a fringe pattern.

4.3 The effect of resonator length fluctuations

Apart from reaching a large finesse, mechanical stability is always a concern when constructing an interferometer. In practice, the round-trip time in any resonator without active element continuously varies around its mean value because of two main reasons. The first is the mechanical vibrations of the optical elements of the interferometer while the other is due to the ambient air in the laboratory, which can flow slowly and its refractive index can also vary locally due to local temperature variations. These are valid for laser resonators (and this causes the CEP slippage) and for our ring resonator, too. Note that a way to overcome these effects is to build ultra-stable passive cavities, such that the laser round-trip time is locked to them [27] using the Pound–Drever–Hall technique.

The change of relative beam path lengths lies in the range of few tens of nanometers and seldom reaches a micron. This small change has basically one effect, that is, the carrier-envelope phase varies, and eventually an interferogram is obtained with degraded visibility. This effect was simulated by adding a small amount of extra beam path to each pulse

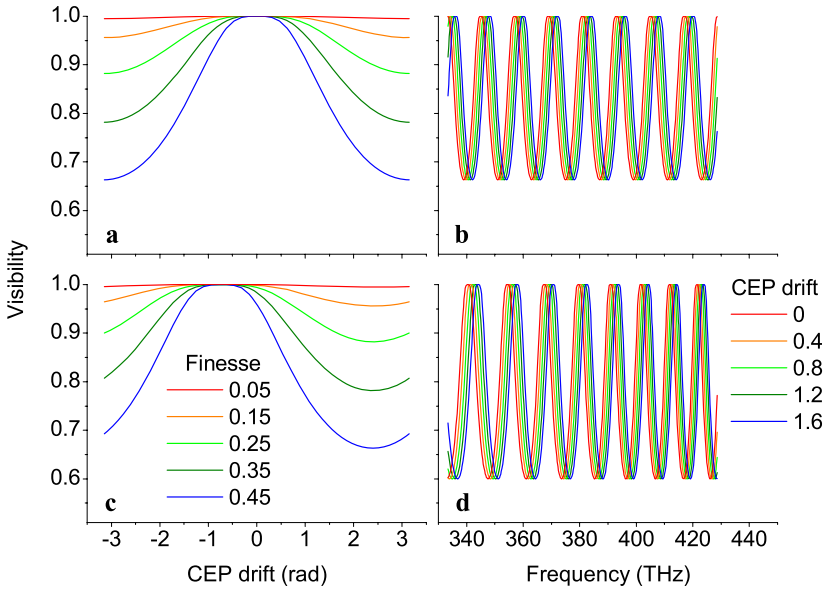

Fig. 6 Influence of air dispersion. (**a**) Matched cavities, vacuum, (**b**) mismatched cavities, $\Delta l = 25$ µm (cf. Fig. 4c), vacuum, (**c**) matched cavity, air, $T = 18°C$, $p = 1.013 \times 10^5$ Pa, 3.43 m path length, (**d**) mismatched cavities, $\Delta l = 25$ µm, air under conditions as in (**c**)

circulating in the resonant ring. The amount of this extra path was chosen randomly within a certain range. As is clear from Fig. 5, the visibility curves are basically unaffected if the resonator length fluctuation is within 20 nm. At larger fluctuations, e.g. for 100 nm (Fig. 5c), the visibility curves are decreasing and at the same time widened around zero CEP drift, as if the nonaffected visibility curve is truncated.

4.4 The effect of ambient air dispersion

A further concern in interferometry is the influence of dispersion, e.g., from atmospheric air. To clarify this influence, we performed simulations assuming vacuum, both for the unmismatched and the mismatched case; see Fig. 6a and b, respectively. These simulations are to be compared with calculations assuming a total path length of 3.43 m in atmospheric air under standard conditions; see Fig. 6c and d, respectively. Quite clearly, air dispersion acts to shift the visibility curves in Fig. 6c by about $\Delta\varphi_{\mathrm{CE}} \approx -1$ rad, as compared to Fig. 6a. A similar shift of about $1/6$ of a free spectral range is observable in the calculations for the mismatched case, Figs. 6b and d. It is therefore clear that the interferometers have to be kept under vacuum if absolute calibration is necessary. On the other hand, however, the observed shift is small enough not to cause strong variations with typical atmospheric pressure variations. Therefore, once calibrated, it can be typically neglected for most applications of our interferometric measurement set-up.

5 Experimental

The above considerations have been verified in an experiment, using a 10 fs Ti:sapphire laser oscillator as the source. The carrier-envelope offset frequency f_{CEO} of this laser was continuously tracked with a standard f-to-$2f$ interferometer, while the repetition rate f_{rep} was accurately monitored by a high precision counter. Using (4), the slippage of carrier-envelope phase can then be determined from f_{CEO} and f_{rep}. Within a measurement series, f_{CEO} was set to five different values by a piezo-controlled intracavity wedge pair within a range of 17 MHz. Between two series, the delay line of the resonant ring was tuned from the case of exact matching of the repetition rate of the oscillator ($\Delta l = 0$) to that of a strong mismatch ($\Delta l = 50$ µm). Between two measurement campaigns the finesse of the resonant ring was also varied by changing the beamsplitters BS_2 and BS_3.

At each step nine SSRI fringes have been captured along with the spectral intensity distribution of the sample and reference arm of the Mach–Zehnder interferometer. The spectral visibility was then calculated for each interferogram, and their average is assigned to the measured particular conditions, that is, to a certain CEP slippage rate, finesse, and delay.

For numerical simulation of the measurement, the spectral reflectivity of each mirror and beamsplitter has been carefully measured within the spectral range of 650–950 nm. From these values the spectral transmittance of both arms as well as the spectrally varying finesse of the resonant ring were calculated. The displayed values of finesse are given at the central wavelength of the pulse. All calculated curves originate from first principle simulations, in which the measured spectral properties of the optical components, the measured f_{CEO} and f_{rep}, the beam path fluctuations due to air flow, the dispersion of ambient air and the exposure time of the camera have additionally been considered.

When the resonant ring is detuned, we expect strong spectral modulation (as in Fig. 4) that depends on CEP drift.

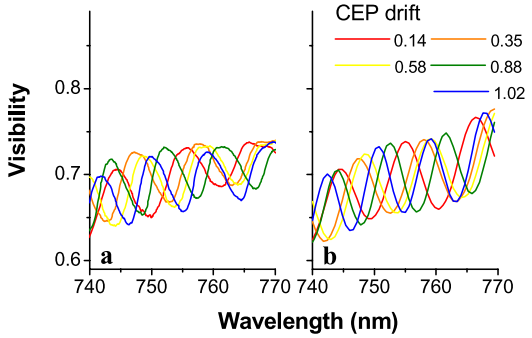

Fig. 7 Measured visibility values vs. wavelength for five different values of the CEP drift rate; ring resonator detuned by $\Delta l = 46$ µm (**a**). Simulation of the measurements (**b**)

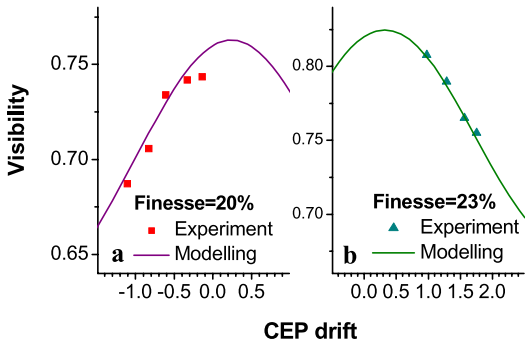

Fig. 8 Visibility of fringe pattern vs. pulse-to-pulse CEP drift of the oscillator at the center wavelength, ring resonator aligned for $\Delta l = 0$ mismatch in the case of two different finesses. Symbols indicate measured values; curves depict results of numerical simulations

The corresponding measured curves are shown in Fig. 7. The agreement between the measured spectral visibilities and the predicted ones is excellent. The only apparent problem is a slight phase shift of the measured curves, which is related to a small residual phase jitter on the order of 100 mrad. This value is also an indication for the achieved accuracy of the measurement.

Figure 8 shows the measured visibility in the function of the measured CEP drift when the resonant ring was rigorously aligned to match the repetition rate of the oscillator ($\Delta l = 0$). For both configurations of the resonant ring with different finesse, the measured visibilities agree very well the calculated curves. With the exception of the data measured at the lowest finesse, deviations between experiment and theory are again well compatible with an error budget of 100 mrad, which translates into an uncertainty of less than 130 kHz in the determination of f_{CEO}.

6 Conclusion

As our method for measuring the CEP drift only relies on linear optics, it is widely independent of power or bandwidth constraints and can therefore be utilized in a much more general way than the f-to-$2f$ interferometer. On the other hand, our linear optical method is certainly not suited for phase tracking and applications in frequency metrology; nevertheless it provides access to the CEO frequency of lasers that cannot be measured with conventional means. This class of lasers includes picosecond lasers, pulsed lasers with rather low peak power as used, e.g., in telecommunication applications. We anticipate that jitter problems will be much less pronounced at higher repetition rates, as the interferometer can be built much more compactly, and also because it appears easier to reach a high finesse in this case. Additionally, environmental influence can be easily reduced by evacuating a compact interferometer set-up. Therefore it appears possible to further push the accuracy of this method into the range of a few 10 mrad.

Of course, there are also bandwidth constraints in our interferometric method. For being able to reliably extract the spectral visibility, the interference fringes have to be resolved at least at some 10 different wavelengths in the spectrograph, which sets a practical limitation for unchirped pulses of many picosecond duration. It is important to understand that this is a bandwidth limitation, i.e., strongly chirped pulses with 100 ps width may still prove measurable. In any case, this limitation is about 1000 times less stringent than in the f-to-$2f$ interferometer. Similarly, there is also a constraint for detection of meaningful interferograms in SSRI, requiring about 10^5 photons on every pixel of the detector array, which typically translates into about one microjoule of cumulated pulse energy for practical interferometry applications. Again, this constraint is less stringent than energy constraints in traditional f-to-$2f$ interferometry [26].

We therefore believe that our linear interferometric method opens a window to an otherwise inaccessible laser parameter for a wide class of mode-locked lasers that either lack sufficient peak power or bandwidth.

Acknowledgements This work has been supported by OTKA under grants TS 49872, K75149 and by the DFG under grant STE 762/5-1. During the project M.G. has held a Deak Ferenc Predoctoral Scholarship of the Hungarian Ministry of Education.

References

1. H.R. Telle, G. Steinmeyer, A.E. Dunlop, J. Stenger, D.H. Sutter, U. Keller, Appl. Phys. B **69**, 327 (1999)
2. D. Jones, S.A. Diddams, J.K. Ranka, A. Stentz, R.S. Windeler, J.L. Hall, S.T. Cundiff, Science **288**, 635 (2000)
3. R. Holzwarth, T. Udem, T.W. Hänsch, J.C. Knight, W.J. Wadsworth, P.S.J. Russell, Phys. Rev. Lett. **85**, 2264–2267 (2000)
4. M. Hentschel, R. Kienberger, Ch. Spielmann, G.A. Reider, N. Milosevic, T. Brabec, P. Corkum, U. Heinzmann, M. Drescher, F. Krausz, Nature **414**, 509–513 (2001)
5. T. Udem, R. Holzwarth, T.W. Hänsch, Nature **416**, 233 (2002)

6. G.G. Paulus, F. Grasbon, H. Walther, P. Villoresi, M. Nisoli, S. Stagira, E. Priori, S. De Silvestri, Nature **414**, 182–183 (2001)
7. T. Udem, R. Holzwarth, T.W. Hänsch, Nature **416**, 233–237 (2002)
8. T.W. Hänsch, Rev. Mod. Phys. **78**, 1297–1309 (2006)
9. S.T. Cundiff, J. Ye, Rev. Mod. Phys. **75**, 325–342 (2003)
10. M. Mehendale, S.A. Mitchell, J.-P. Likforman, D.M. Villeneuve, P.B. Corkum, Opt. Lett. **25**, 1672 (2000)
11. M. Kakehata, H. Takada, Y. Kobayashi, K. Torizuka, H. Takamiya, K. Nishijima, T. Homma, H. Takahashi, K. Okubo, S. Nakamura, Y. Koyamada, Opt. Express **12**, 2070–2080 (2004)
12. J.M. Dudley, S. Coen, Opt. Lett. **27**, 1180–1182 (2002)
13. F.W. Helbing, G. Steinmeyer, U. Keller, R.S. Windeler, J. Stenger, H.R. Telle, Opt. Lett. **27**, 194 (2002)
14. T.M. Fortier, J. Ye, S.T. Cundiff, R.S. Windeler, Opt. Lett. **27**, 445–447 (2002)
15. O.D. Mücke, R. Ell, A. Winter, J.-W. Kim, J.R. Birge, L. Matos, F.X. Kärtner, Opt. Express **13**, 5163–5169 (2005)
16. T. Fuji, J. Rauschenberger, A. Apolonski, V.S. Yakovlev, G. Tempea, T. Udem, C. Gohle, T.W. Hänsch, W. Lehnert, M. Scherer, F. Krausz, Opt. Lett. **30**, 332–334 (2005)
17. B.R. Washburn, S.A. Diddams, N.R. Newbury, J.W. Nicholson, M.F. Yan, C.G. Jorgensen, Opt. Lett. **29**, 250–252 (2004)
18. L. Xu, C. Spielmann, A. Poppe, T. Brabec, F. Krausz, T.W. Hänsch, Opt. Lett. **21**, 2008 (1996)
19. K. Osvay, M. Görbe, C. Grebing, G. Steinmeyer, Opt. Lett. **32**, 3095 (2007)
20. C. Sainz, J.E. Calatroni, G. Tribillon, Meas. Sci. Technol. **1**, 356 (1990)
21. A.P. Kovács, K. Osvay, Zs. Bor, R. Szipőcs, Opt. Lett. **20**, 788 (1995)
22. K. Osvay, P. Dombi, A.P. Kovács, Z. Bor, Appl. Phys. B **75**, 649 (2002)
23. A.P. Kovács, K. Osvay, G. Kurdi, M. Görbe, J. Klebniczki, Z. Bor, Appl. Phys. B **80**, 165 (2005)
24. D. Meshulach, D. Yelin, Y. Silberberg, J. Opt. Soc. Am. B **14**, 2095–2098 (1997)
25. A. Börzsönyi, A.P. Kovács, M. Görbe, K. Osvay, Opt. Commun. **281**, 3051 (2008)
26. S. Koke, C. Grebing, B. Manschwetus, G. Steinmeyer, Opt. Lett. **33**, 2545 (2008)
27. R.J. Jones, I. Thomann, J. Ye, Phys. Rev. A **69**, 051803 (2004)